Research Article Vol. 14, No. 9 / 1 Sep 2023 / *Biomedical Optics Express* 4888

Biomedical Optics EXPRESS

Non-invasive *in vivo* imaging of human corneal microstructures with optical coherence microscopy

HADIYA F. PATTAN,[1] XIAO LIU,[1] AND PATRICE TANKAM[1,2,*]

[1] *School of Optometry, Indiana University, Bloomington, IN, 47405, USA*
[2] *Intelligent Systems Engineering, Luddy School of Informatics, Computing, and Engineering, Indiana University, Bloomington, IN, 47405, USA*
[*] *ptankam@iu.edu*

Abstract: Non-invasive imaging systems with cellular-level resolution offer the opportunity to identify biomarkers of the early stage of corneal diseases, enabling early intervention, monitoring of disease progression, and evaluating treatment efficacy. In this study, a non-contact polarization-dependent optical coherence microscope (POCM) was developed to enable non-invasive *in vivo* imaging of human corneal microstructures. The system integrated quarter-wave plates into the sample and reference arms of the interferometer to enable deeper penetration of light in tissues as well as mitigate the strong specular reflection from the corneal surface. A common-path approach was adopted to enable control over the polarization in a free space configuration, thus alleviating the need for a broadband polarization-maintained fiber. The POCM achieved volumetric imaging of corneal microstructures, including endothelial cells over a field of view 0.5×0.5 mm^2 with an almost isotropic resolution of ~2.2 µm and a volume (500 × 500 × 2048 voxels) rate of 1 Hz. A self-interference approach between the corneal surface and underlying layers was also developed to lessen the corneal curvature and axial motion artifacts, thus enabling high-resolution imaging of microstructures in the anterior cornea, including squamous epithelial cells, wing epithelial cells, basal epithelial cells, sub-basal nerve plexus, and stromal keratocytes.

1. Introduction

Although transparent, the cornea consists of well-organized microstructures that contribute to its homeostasis and function and its shape provides two-thirds of the optical power of the eye. This outermost element of the visual system is at risk of infections and other environmental factors. It is also vulnerable to a multitude of pathological conditions, including keratoconus, dry eye, and Fuchs endothelial corneal dystrophy (FECD), which can compromise the cornea's integrity and function, leading to vision loss or even blindness. Keratoconus is a multifactorial disease that causes the cornea to locally thin and bulge into a cone shape, resulting in asymmetric astigmatism and impaired visual acuity [1]. Although the etiology of keratoconus remains unknown, recent studies have reported the damage of corneal nerves associated with the rupture of the Bowman's layer within the keratoconic area, leading to a direct interaction between epithelial cells and keratocytes [2]. This finding raised the possibility that nerve injury and altered sensation may be involved in the progression of the disease [3]. FECD on the other hand is an hereditary disorder that affects the corneal endothelium causing a progressive loss of endothelial cells and in most cases the excrescences of the Descemet's membrane called guttae [4]. This condition progressively causes the entire cornea to swell leading to corneal edema, altered epithelial cells, and corneal nerves [5,6]. Changes in keratocytes' density and reflectivity have also been reported in corneas with FECD [7–9]. In addition to these diseases, contact lens wear can affect the cornea integrity in several ways, including the thickness and morphology of the corneal epithelium, the

#495242 https://doi.org/10.1364/BOE.495242
Journal © 2023 Received 31 May 2023; revised 6 Aug 2023; accepted 16 Aug 2023; published 25 Aug 2023

integrity of meibomian gland, as well as the sensitivity of corneal nerves, especially in people with pre-existing corneal conditions or altered ocular surfaces such as dry eye [10,11].

Non-invasive imaging technologies that can identify biomarkers of the early stage of corneal infection and disease with cellular-level resolution offer the opportunity to advance our understanding of disease and enable early intervention and monitoring. Advancements in *in vivo* confocal microscopy (IVCM) and optical coherence tomography (OCT) have greatly enhanced our ability to detect and describe cellular characteristics of a multitude of corneal pathologies [12,13].

IVCM can produce high-resolution images of biological tissues and has developed into a vital clinical tool in several disciplines, including ophthalmology [14,15]. The advantages of IVCM include the capacity to image all layers of the cornea with cellular-level details [16,17]. IVCM, however, comes with certain drawbacks including the low acquisition speed and the need for ocular lubrication to optically couple the microscopic objective lens with the cornea [18]. This contact with the ocular surface not only causes discomfort for patients but also potentially disrupts the natural organization of corneal structures and especially corneal nerves through the activation of mechanotransduction pathways [19]. Also, the lack of a real-time cross-sectional view of the cornea during image acquisition makes it difficult to align the microscopic objective lens with the cornea and identify the shallow focusing depth location of the beam in the tissue. Moreover, a highly trained professional operator is often necessary [20–24].

OCT on the other hand can produce non-contact three-dimensional (3D) images of tissues with micrometer-scale axial resolution [25–29]. OCT offers several advantages over IVCM, including its high acquisition speed, non-invasiveness, real-time display of cross-sectional images of the cornea, the ability to capture images of all layers of the cornea in a single shot as well as provide an accurate evaluation of the corneal thickness and curvature [30,31]. However, the non-contact benefit of OCT comes at the expense of motion artifacts that need to be addressed through subject stability and increased frame rate [30]. Moreover, OCT usually operates with a low numerical aperture (N.A.) objective lens, yielding images with poor cellular details compared to IVCM [32].

Optical coherence microscopy (OCM) was introduced as a solution for combining the high axial resolution of OCT and the high lateral resolution of IVCM through the use of high N.A. objective lenses in OCT [33] and has been revealed as a viable technique for imaging microstructures of the human cornea [34–37]. Full-field OCM (FF-OCM) operates in a similar manner as IVCM by illuminating the cornea with a collimated beam of light [13]. FF-OCM uses the coherence property of light to section different depths of the cornea by moving the reference mirror of the interferometer [35] instead of the sample/objective lens as is the case in IVCM. FF-OCM also shares some drawbacks with IVCM including the lack of real-time visualization of cross-sectional images of the cornea, which can be mitigated by integrating FF-OCM with spectral-domain OCT [38]. Spectral-domain OCM (SD-OCM) overcomes some of the drawbacks of IVCM/FF-OCM and OCT by enabling real-time cross-sectional images of the cornea with a cellular-level resolution, thus offering a fast thorough assessment of corneal microstructures at different depths [39].

In this study, we developed a new approach of SD-OCM, polarization-dependent optical coherence microscopy (POCM), in which the polarization property of light was leveraged to enable the visualization of all layers of the human cornea *in vivo*. The polarization property of light has been previously used in polarization-sensitive OCT (PS-OCT) and cross-polarization OCT (CP-OCT) to evaluate the birefringence or depolarization property of tissues as well as changes due to pathological conditions [40,41]. Unlike PS-OCT and CP-OCT, the proposed POCM uses the polarization of light to enhance the contrast of cellular features that are not birefringent, especially in samples with highly reflective surfaces such as the cornea. The strong specular reflection from the corneal surface is a common challenge in corneal imaging [42], which generally compromised the collection of backscattered light from underlying structures including epithelial cells. The self-interference between the corneal surface and underlying layers was also developed to produce high-contrast imaging of human corneal epithelial cells and the sub-basal nerve plexus.

2. Methods

2.1. Design of the polarization-dependent optical coherence microscope

Figure 1 presents the prototype of POCM that was designed for *in vivo* human corneal imaging. The system was powered by a partially polarized near-infrared (NIR) super luminescent diode source (M-T-850-HP-I, Superlum, Ireland) with a central wavelength of 850 nm and a bandwidth of 165 nm, enabling a theoretical axial resolution of 1.9 µm in air. The partially polarized light source was adopted to enable the evaluation of the polarization-dependent contrast. The light source was transmitted to the interferometer through a 1×2 fiber coupler (TW850R5A1, Thorlabs, Newton, NJ) and a 4–mm aperture fiber collimator (F280APC-850, Thorlabs, Newton, NJ). This common-path approach was adopted to enable control over the polarization in a free space configuration, thus mitigating the need for a broadband polarization-maintained fiber at 850 nm, as well as the system's instability due to the optical path length shift between the two arms of the interferometer. A polarization controller was integrated into the common-path fiber to adjust the polarization state of the incoming light so that its dominant polarization is horizontal, allowing optimization of the relative contribution of linear and nonlinear polarization portions of the light source. A 30:70 (R:T) non-polarizing beam splitter (BS020, Thorlabs, Newton, NJ) was used to split the light into the sample and reference arms. A quarter-wave plate (QWP) (#46-560, λ/4 Achromatic Waveplate, Edmund Optics, Barrington, NJ) angled at 45° from the horizontal axis (i.e., dominant polarization) was integrated into the sample arm to turn the horizontal and non-horizontal linear polarizations into circular and elliptical polarizations, respectively. This configuration enabled light to penetrate deeper into tissues [43]. A similar QWP with the fast axis adjustable between 0 and 45° relative to the fast axis of the sample arm QWP was integrated into the reference arm to selectively enable interference of either linear or non-linear polarization states. The dispersion between the two arms was compensated using a combination of dispersion compensation elements – DCE (LSM54DC1, Thorlabs, Newton, NJ), a diffraction grating – DG (GR25-0608, Thorlabs, Newton, NJ), an achromatic doublet – ACD1 (AC254-030-B, Thorlabs, Newton, NJ), and a flat mirror – M (PFSQ10-03-P01, Thorlabs, Newton, NJ) [44]. This was achieved by directing the +1 order of the diffracted beam toward the outer half-portion of the lens ACD1, thus allowing individual wavelengths to experience different optical paths inside the lens material [45]. The reference arm was mounted on a manual translation stage (TBB0606, Thorlabs, Newton, NJ), enabling the control of the optical path length difference of the interferometer. The sample arm included a dual-axis galvanometer scanner (GVSK2-US, Thorlabs, Newton, NJ) and a 2.5X telescopic relay system using a 30-mm (ACD2) and 75-mm (ACD3) achromatic doublets (#49-352 and #45-805, Edmund Optics, Barrington, NJ) to conjugate the midway position between the scanning mirrors (distant by 10 mm) with the back focal plane of the microscopic objective and expand the beam so that it overfills the 10–mm back aperture of the 10X microscopic objective (#86-818, Olympus UPLFLN 10x, 0.30 NA, Edmund Optics, Barrington, NJ), yielding a theoretical lateral resolution of 1.7 µm at 850 nm according to the Rayleigh criterion. The interference signal was recorded with a customized spectrometer (Cobra–S 800, Wasatch Photonics, Morrisville, NC), equipped with a 250kHz line-scan camera (Octoplus 2 k, Teledyne e2v, England) and connected to a frame grabber (AXN-PC2-CL-1xE, Bitflow, Woburn, MA), enabling an imaging depth of ~1 mm with a sensitivity greater than 97 dB. The synchronization between the scanners and the frame grabber was achieved through a four-channel analog output data acquisition card (NI USB-6363, National Instruments, Austin, TX). The imaging system was assembled on a 12" x 12" aluminum breadboard that was mounted on a three-axis manual translation stage to enable the alignment of the system with the human eye. The system also integrated a bite bar, a headrest, and an in-line fixation target to stabilize the participant's head during imaging (Fig. 1(b)).

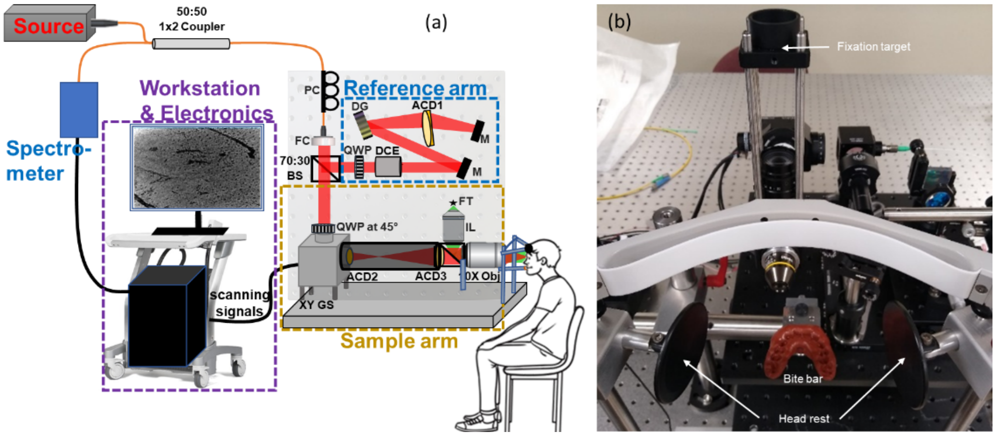

Fig. 1. Schematic of POCM for in vivo human corneal imaging. PC, polarization controller; FC, fiber collimator; QWP, quarter-wave plate; DCE, dispersion compensation elements; DG, diffractive grating; M, mirror; ACD, achromatic doublet; 10X Obj, 10X-microscopic objective; BS, beam splitter; FT, fixation target; IL, imaging lens.

2.2. Protocol for human corneal imaging

Two subjects were recruited for this study. The enrollment criteria include subjects within the age range of 18 to 35 years who have undergone an eye exam within the last 12 months and have no history of eye diseases, eye surgery, or eye injury. The protocol for imaging human subjects with POCM was approved by Indiana University's Human Subjects & Institutional Review Boards (IRB). Informed consent was obtained from each subject before the imaging session. All procedures conformed to the tenets of the Declaration of Helsinki for biomedical research involving human subjects. A bite bar mold was made for each subject using the Kerr Impression compound (Thermoplastic impression material, 1236714, Henry Schein, NY), which was mixed according to the manufacturer's instructions. The impression compound was dissolved in boiled lukewarm water, to prevent the material from sticking to the teeth, and filled onto an aluminum plate. The aluminum plate with the impression material was placed in the subject's mouth and once the material was centered and stable, the subject was instructed to bite down on the impression material, applying even pressure on both sides. The mold was set for a few minutes to become rigid before being mounted on the bite bar for POCM imaging. A two-side headrest was integrated into the system to stabilize subjects' heads during imaging and reduce motion artifacts. For the imaging session, subjects were comfortably seated on a chair in front of the system and instructed to bite on their mold. The two-side headrest was placed against the right and left side of the forehead to keep the head as stable as possible during imaging (Fig. 1). The headrests were secured using tightening screws without causing discomfort to the subject. Only the left eye of each subject was imaged while the right eye was patched to improve the fixation of the target. The POCM's scanning head was then moved closer to the subject's eye (10 mm working distance) using a three-axis manual translation stage. A real-time 2D scan display was used to monitor the alignment of the scanning head with the subject's eye and adjust the plane of focus of the POCM beam. The subject was instructed to fixate on the target during the acquisition of individual volumes. A series of four volumes were collected at each depth of the cornea to increase the likelihood of collecting images free of motion artifacts. The acquisition time of individual volumes was 1 second. Each imaging session lasted for about 30 minutes: 5 minutes for the informed consent, 10 minutes for making the mold, and 15 minutes for POCM imaging. Note that the instrument operated in a non-contact mode with a 10-mm working distance limiting any risks of touching the cornea or causing any corneal injuries or infections. Furthermore, the incident power onto the cornea was below 2 mW, which was well below the threshold for thermal tissue damage and *in vivo* eye safety by ANSI (American National Standards Institute) [46]. In addition, the beam focusing onto the cornea will be well spread out when it reaches the retina, further reducing the risk of phototoxicity to the retina. The imaging protocol was similar for both subjects, with the only difference being the relative orientation of the QWP in the reference arm. For the first subject, the fast axis of the reference QWP was set at 45° relative to the fast axis of the sample QWP (cross-polarization) whereas it was set at 0° for the second subject (co-polarization).

2.3. *Data Acquisition and Processing*

Several strategies were used to overcome motion artifacts inherent to *in vivo* human imaging. First, the field of view was reduced from 1×1 mm^2 to 0.5×0.5 mm^2, thus reducing the sampling points from 1000×1000 Ascans to 500×500 Ascans, yielding a four-time reduction in the acquisition time of individual POCM volumes (from 4 seconds to 1 second). Although this modification induced a lower signal-to-noise ratio, it did not have a significant impact on the image quality. Another strategy for overcoming the axial motion of the eye was by leveraging the self-interference signal between the corneal surface and underlying corneal layers, enabling high-contrast images of cellular features of the anterior cornea. Both images from the self-interference and the interference between the reference arm and the sample were simultaneously captured and distinctly displayed at different depth locations in the same image enabled by the shallow depth of focus of OCM. One benefit of self-interference in POCM is that it enables imaging of the anterior cornea with the highest axial resolution enabled by the source and detector, free of dispersion that usually degrades the axial resolution due to the mismatch of optical components between the reference and sample arms. Custom programs in LabVIEW 2017 (National Instruments, Austin, TX) and MATLAB (The Mathworks, Natick, MA) were developed for data acquisition and processing. A flattening algorithm was applied to data sets to numerically remove the curvature of the cornea and correct for the axial motion artifacts, thus enabling the visualization of cellular features in enface images [37,45]. It is worth noting that the self-interference portion of the images needed no flattening as the corneal curvature and axial motion artifacts were intrinsically compensated. The free open-source image-processing platform ImageJ was used for image analysis.

3. Results

3.1. *POCM calibration and testing*

We have previously reported on the axial and lateral resolutions of OCM systems with similar specifications [45], and we were interested in investigating the effect of polarization and reduced sampling on the resolutions of the system. The axial resolution was evaluated by imaging a thin glass with a thickness of ~150 µm set as the sample. The point spread function (PSF) of the system was evaluated in three configurations of the relative angle between the fast axes of the reference and sample QWPs set at 0, 22.5°, and 45°. Figure 2 presents the interference signals and corresponding depth profiles in the three configurations while focusing onto the front surface of thin glass.

Note that the specular reflection from the highly reflective front surface of the glass located at Δz was reduced by almost 100% by changing the relative angle between the two QWPs from 0°

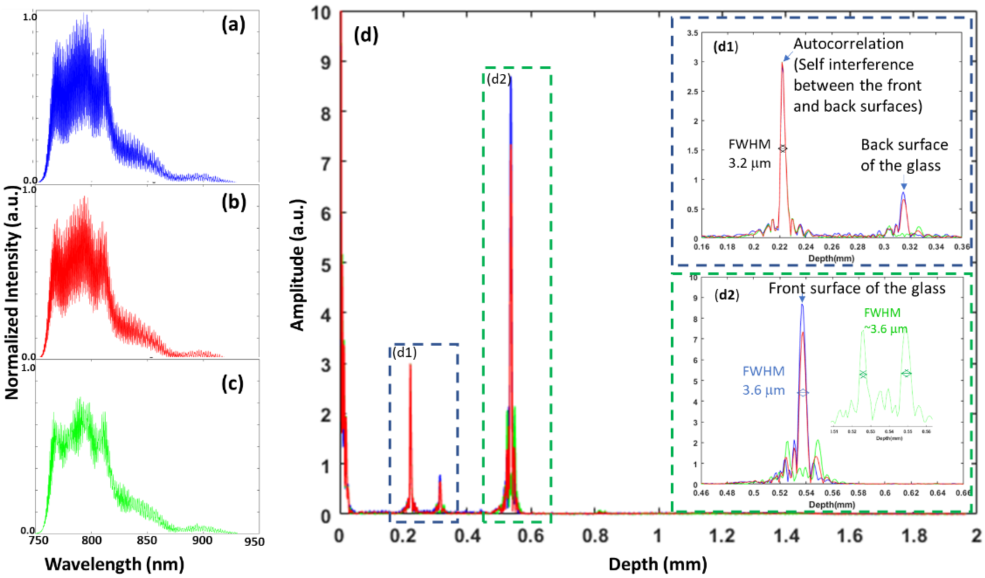

Fig. 2. Interference signals in three different arrangements of the reference arm quarter-wave plate (QWP) with the fast axis of the QWP in the sample arm set at 45° from horizontal. (a) Interference signal with the relative angle of 0° between QWPs (blue trace). (b) Interference signal with the relative angle of 22.5° between QWPs (red trace). (c) Interference signal with the relative angle of 45° between QWPs (green trace). (d) Corresponding depth profiles of the three configurations. The inserts highlight depth profiles in the three configurations corresponding to the point spread function (PSF) from the self-interference between the front and back surface of the glass (d1) and the PSF from the interference with the reference arm (d2).

(blue traces) to 45° (green traces) (Fig. 2). In the latter, the polarizations of incident co-linear electric fields in the reference and sample arms of the interferometer became orthogonal after the round trip through the QWPs, assuming no depolarization occurred in the sample, resulting in destructive interference. The image of the sample was therefore formed from the interference between non-linear polarization states [47], which yielded the emergence of two peaks symmetric around Δz (see the green trace inserted in Fig. 2(d2)). This was likely due to the phase shift between right elliptically polarized and left elliptically polarized electric fields in the reference arm interfering with elliptical electric fields in the sample arm [48]. This false double-peak will cause individual layers to be replicated at a different depth (ghost image), slightly degrading the contrast of individual layers. Nevertheless, the FWHMs of these peaks were comparable to that of the configuration at 0° (Fig. 2(d2)) and will produce a similar depth sectioning of the sample. The measured axial resolution of 3.2-3.6 µm in air was higher compared to the theoretical value of 1.9 µm, mostly due to the chromatic shift of the microscopic objective lens as well as its low transmission in the longer wavelength range. The chromatic dispersion contributed to ~0.4 µm of this axial resolution degradation.

To evaluate the impact of the reduced sampling points and polarization on the lateral resolution and field of view of POCM, a positive non-fluorescent USAF 1951 resolution test chart (R1L1S1P, Thorlabs, USA) was imaged in four different configurations, including a combination of 1000 × 1000 A-scans, 500 × 500 A-scans, and relative angle of the reference arm QWP set at 0° and 45°. Figure 3 shows the *enface* POCM images and line profiles across the 6th elements of the 7th group of the test chart in the four configurations.

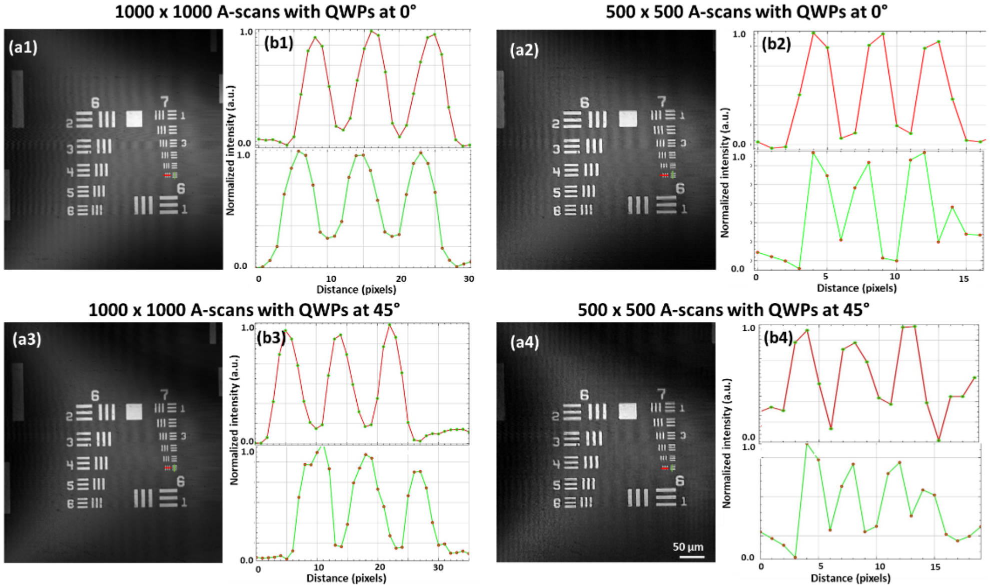

Fig. 3. POCM Enface images of the resolution chart over a field of view of 0.5×0.5 mm^2 with the corresponding intensity profiles over the 6th elements (horizontal and vertical orientations) of the 7th group in four configurations. (a1) 1000×1000 A-scans with the relative angle of QWPs set at 0ˆ. (b1) Corresponding intensity profiles. (a2) 500×500 A-scans with the relative angle of QWPs set at 0ˆ. (b2) Corresponding intensity profiles. (a3) 1000×1000 A-scans with the relative angle of QWPs set at 45ˆ. (b3) Corresponding intensity profiles. (a4) 500×500 A-scans with the relative angle of QWPs set at 45ˆ. (b4) Corresponding intensity profiles.

While the definition of the image was better with 1000 sampling points, the system could still resolve the finest elements of the chart with 500 sampling points, which still satisfied the Nyquist sampling requirement over a field of view (FOV) of 0.5×0.5 mm^2. Thus, this reduced sampling did not affect the lateral resolution of the system. The system operating with 500 sampling points was able to resolve the 6th elements of the 7th group, corresponding to a lateral resolution of 2.2 µm, and was adopted for *in vivo* human imaging.

3.2. In vivo POCM imaging of the human cornea

Figure 4 presents cross-sectional and enface images of the cornea of the two subjects evaluated in this study. Note that the cross-sectional images (Figs. 4(a1) and 4(a2)) are for illustration purposes and were not extracted from the same volumes used for *enface* images. Similarly, *enface* images were extracted from different POCM volumes as it was necessary to focus the beam at different depth of the cornea between acquisitions.

Note that the cross-sectional image from Subject 1 captured with the relative angle of 45° between the QWPs exhibits a false double-layer of the ocular surface with an overall low signal (Fig. 4(a1)) whereas the image from Subject 2 captured with the relative angle of 0° between the QWPs exhibits a strong specular reflection from the surface. Both images from the interference between the cornea and the reference arm of POCM (top part of the image) and from the self-interference between the corneal surface and underlying structures (bottom part of the image) are distinctly represented in the images (Figs. 4(a1) and 4(a2)). The self-interference was not affected by the axial motion as long as the amplitude of the motion remained within the depth of focus of the objective lens. *Enface* images of the corneal surface (Figs. 4(b1) and 4(b2)) exhibit

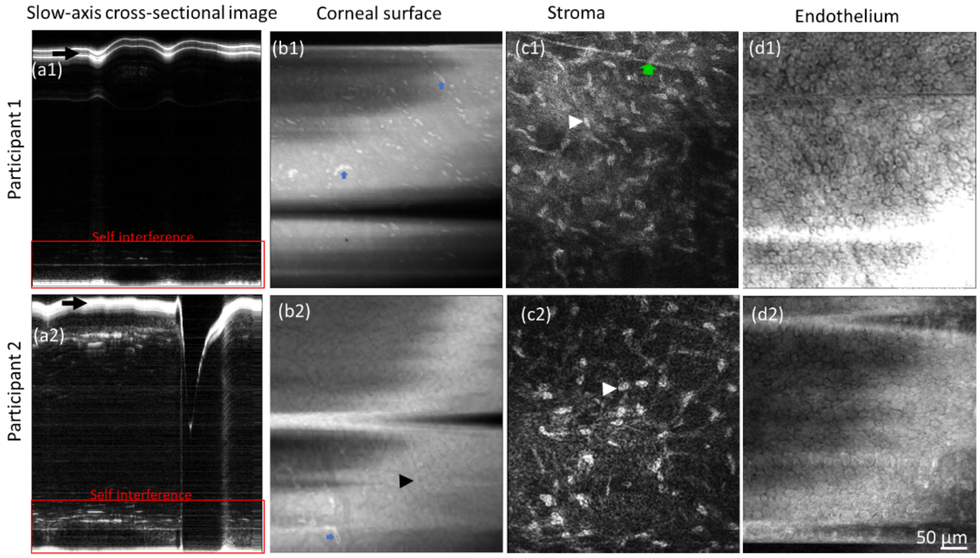

Fig. 4. POCM images of the cornea in two healthy subjects. (a1) and (a2) Cross-sectional images along the slow-scanning axis of Subjects 1 and 2, respectively, showing the axial motion as well as a blink (gap in (a2)) during the acquisition. (a1) exhibits a false double-layer of the surface induced by the configuration with QWPs at 45ˆ whereas (a2) shows a strong specular reflection from the surface in the configuration with QWPs at 0ˆ (black arrows). The top part of the image corresponds to the interference of the cornea with the reference arm whereas the botom part corresponds to the self-interference, which is not affected by the axial motion. (b1) and (b2) *Enface* images of the corneal surface of Subjects 1 and 2, respectively. Hyperreflective features (blue arrows) are visible on the surface, presumably immune cells or infiltrates from the tear film. Low-contrast squamous epithelial cells and their hyporeflective nuclei (black arrowhead) are also visible in (b2). (c1) and (c2) *Enface* images of the mid-stroma showing keratocytes (white arrowheads) as well as a nerve branching (green arrow). (d1) and (d2) *Enface* images of the endothelium showing endothelial cells.

squamous epithelial cells (black arrowhead) as well as hyperreflective features (blue arrows), presumably immune cells or infiltrates from the tear film. The significance of these features will be worth further investigation. While both configurations of the QWPs produced high-contrast images of the stroma (Figs. 4(c1) and 4(c2)), the contrast was reduced with the 45° configuration. Also, the induced double-layer feature may cause an overestimation of the density of keratocytes. Thus, this configuration may be more suitable for imaging the corneal surface, epithelial cells, and endothelial cells.

Figure 5 shows *enface* images of the anterior cornea extracted from the self-interference portion of the volumes (see Figs. 4(a1) and 4(a2) for illustration).

These results provide valuable insights into key microstructural features of the anterior cornea and highlight the potential of self-interference-based POCM as a powerful tool for non-invasive in vivo imaging of the ocular surface. The self-interference portion of POCM images enables to delineate between all layers of the anterior cornea with the highest axial resolution, free of chromatic dispersion. Even more importantly, the self-interference enables to overcome the curvature of the cornea as well as axial motion artifacts that compromised the visualization of cellular features, especially the corneal sub-basal nerve plexus, in a single *enface* image. These findings have important clinical implications for the early detection and management of corneal diseases and pave the way for numerous longitudinal studies, involving the anterior cornea, such

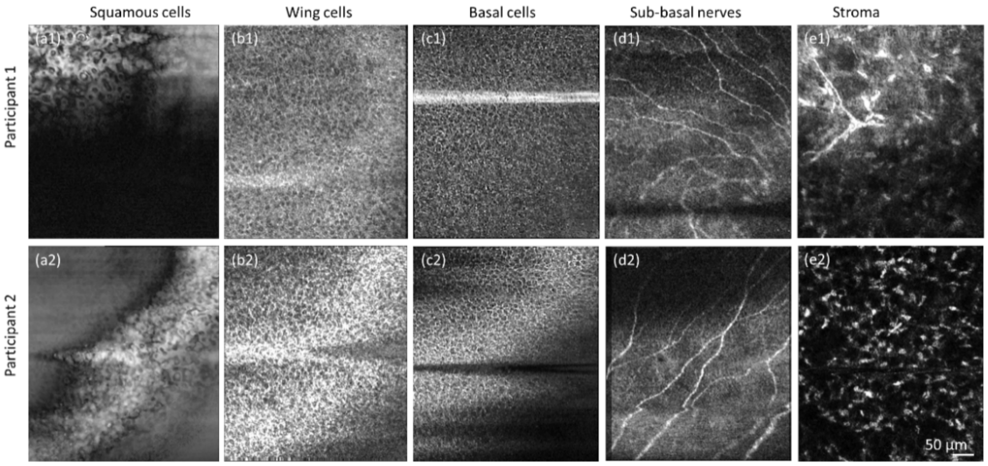

Fig. 5. POCM images of the anterior cornea of the two subjects from the self-interference region in Fig. 4. (a1) and (a2) *Enface* images of squamous epithelial cells in both subjects showing some hyporeflective nuclei and cell boundaries. (b1) and (b2) *Enface* images of wing epithelial cells in both subjects. (c1) and (c2) *Enface* images of basal epithelial cells in the two subjects. (d1) and (d2) *Enface* images of sub-basal nerve plexus. (e1) and (e2) *Enface* images of the anterior stroma exhibiting keratocytes and a nerve branching in (e1).

as evaluating the impact of the long-term use of contact lenses on the ocular surface, identifying biomarkers of the early stage of keratoconus as well evaluating the efficacy of corneal collagen cross-linking treatment.

4. Discussion

IVCM has long been a standard of care for in vivo human corneal imaging. However, its broader adoption in clinical practices has been challenging due to numerous limitations discussed in this manuscript, to the point where key IVCM suppliers are no longer servicing their systems. Hence, only very few centers have a functional IVCM. With its competitive axial resolution and three-dimensional capabilities, SD-OCM has the potential to outperform and replace the IVCM technology as a standard of care for non-contact human corneal imaging with cellular-level resolution. However, the conventional SD-OCM comes with several shortcomings, including the speed limit, the susceptibility to the strong specular reflection from the corneal surface, the motion artifacts due to involuntary eye movement, and the curvature of the cornea, as discussed in previous studies [36,37]. In this work, we developed strategies to overcome several shortcomings inherent to cellular resolution *in vivo* imaging of the human cornea using SD-OCM. The proposed POCM operated at a fast speed of 1 volume ($500 \times 500 \times 2048$ voxels) per second to overcome eye movements and motion artifacts. The integration of a QWP into the sample arm enabled the illumination light to be elliptically polarized, yielding deeper penetration and increased scattering efficiency in tissues [43]. The integration of a QWP with variable orientations into the reference arm enabled different polarization states to contribute or not to the image formation process. This approach was used to mitigate the strong specular reflection from the corneal surface and therefore enhance the contrast of different layers of the human cornea *in vivo*. While this cross-polarization configuration was not optimized to produce images with contrast as high as the co-polarization configuration, the former revealed some benefits of the use of partially polarized light sources in OCT. Although partially polarized light sources have been reported to degrade the axial resolution of OCT [49], this feature can be beneficial in certain applications given specific arrangements of the polarization states between both arms of the interferometer and will be worth further investigation. As the degree of polarization of the source decreases, the probability of interference between non-linear polarization states would increase [50] and may yield better sensitivity and image contrast. One could consider investigating the optimal degree of polarization of the light source that would yield the desired image contrast. Different strategies for overcoming the false double-layered image (“ghost image”) induced by non-linear polarizations will be investigated in future work. Also, the sensitivity of the system can be further improved by collecting light from the fourth face of the beam splitter, which is currently unused.

POCM was capable of generating depth-resolved images of all corneal layers, including squamous, wing, and basal epithelial cells, corneal sub-basal nerve plexus, stromal keratocytes, as well as endothelial cells, with lateral and axial resolutions of 2.2 µm and ~2.4 µm in the cornea, respectively, and clarity comparable to IVCM. POCM has the advantage over IVCM of being non-contact and providing high depth-sectioning and real-time visualization of cross-sectional images of the cornea, which can enable to delineate all layers of the cornea, including the tear film [38].

Another key advantage of this system is that it enabled high-resolution images of the anterior cornea by using self-interference between the corneal surface and underlying layers. Thus, producing non-invasive and non-contact images of the human cornea with the highest axial resolution enabled by the source and detector, free of dispersion mismatch degradation. Furthermore, this approach overcomes two major challenges in visualizing cellular microstructures of the cornea: 1) the corneal curvature that generally compromises the visualization of cells in a single enface image and requires to numerically flatten the cornea, and 2) image artifacts due to the axial motion of the eye during the acquisition. This feature offers tremendous research opportunities in the anterior cornea, including 1) understanding the dynamics of epithelial cells in healthy and pathological conditions such as keratoconus, 2) evaluating the interaction between contact lenses, the tear film, and the ocular surface, and 3) evaluating corneal nerves in different disease conditions or the impact of long-term wear of contact lenses on the ocular surface. Further development of this approach for clinical settings will offer ophthalmologists and clinicians the opportunity to thoroughly examine corneal cellular structures with great cellular details and track structural changes associated with disease over time, thus providing valuable information about their pathogenesis and treatment efficacy.

Despite the promises of POCM, several limitations to the current system are yet to be addressed to establish its utility in clinical practices.

While the self-interference approach allowed mitigating the axial motion artifacts, artifacts from transverse motion were still present in the images and will require further hardware optimization and the implementation of an additional post-processing algorithm to correct for residual motion artifacts. A cross-correlation approach between successive B-scans of the volume will be developed to compensate for transversal motion artifacts.

Further improvements to POCM for clinical settings include 1) integrating a 2D near-infrared camera to visualize the cornea and enable a fast alignment of the system with the eye, and 2) integrating a three-axis motorized stage into the system for an automatic eye alignment based on the feedback loop from the 2D camera.

Although the images reported here were limited to 0.5×0.5 mm^2 to increase the imaging speed and overcome motion artifacts, the system was capable of a FOV of 1.3×1.3 mm^2, which can be leveraged in applications where a larger FOV is needed. The number of sampling points should then be increased to fulfill the Nyquist sampling requirement and preserve the resolution of the system, which will lower the acquisition speed. The speed of the system can be further improved by upgrading the spectrometer with a faster line-scan camera [51] or integrating a second spectrometer into the system to enable a tandem acquisition between two spectrometers [52], further reducing the acquisition time by a factor of at least two to enable motion-artifact-free images of the human cornea. Another strategy for overcoming the speed limitation in SD-OCT has been through the parallel acquisition of Ascans using line-field SD-OCT [45] or Fourier-domain full-field-OCT [37], which come with their limitations for human corneal imaging such as lower sensitivity and cross-talk. Most importantly, a collimated beam onto the cornea will result in a focused beam on the retina, thus increasing the risk of retinal phototoxicity.

Different strategies for stabilizing the subject head and reducing the motion artifacts were investigated. The bite bar combined with the headrest and the in-line fixation target provided an optimal and cost-effective solution for minimizing the motion artifacts. Although the bite bar can be a little uncomfortable for some subjects, imaging with a bite bar provided greater stability and minimal motion artifacts compared to imaging without a bite bar. Subjects were less prone to unintentional movements of their head when biting on the bite bar.

Another limitation of POCM using the cross-polarization configuration was the reduced signal-to-noise ratio resulting in low-contrast images. Although this limitation did not significantly impact the image quality in the current study, it may affect the visualization of subtle cellular features in certain applications. Further optimizations of the QWPs configurations will be required to improve the image quality.

Imaging the fine structures of the cornea requires micrometer-scale axial and lateral resolutions (high N.A. lenses), resulting in a shallow depth of imaging ($\sim 60\ \mu m$ for POCM with the use of a 10X microscopic objective lens) and limiting the ability to image the entire corneal thickness in a single shot. One mitigation approach to extend the imaging depth of POCM will be to equip the system with a dynamic focusing capability [53], a tunable deformable membrane [54], using a Bessel beam illumination [55], or a computational approach [56].

The self-interference approach enabled to overcome the corneal curvature and axial motion artifacts but is limited to imaging the anterior portion of the cornea using the corneal surface as a reference. Furthermore, this approach requires a smooth and uniform corneal surface, which may not be guaranteed in certain disease conditions such as keratoconus and dry eye. Future studies will investigate the possibility of imaging the posterior cornea using the self-interference approach with the endothelium as a reference, which will provide a valuable tool for in vivo investigation of biomarkers of the early stage of FECD.

5. Conclusion

The proposed POCM enabled non-invasive and non-contact *in vivo* imaging of all layers of the human cornea with a cellular-level resolution, which offers tremendous opportunities to evaluate structural alterations that take place in different corneal diseases early in the disease process as well as monitor the disease progression and evaluate treatment efficacy. POCM has the potential to become a viable clinical tool for ophthalmologists, clinicians, and researchers to thoroughly examine the cornea in normal and pathological conditions.

Funding. CooperVision, Inc.

Acknowledgments. The authors would like to thank CooperVision for the financial support as well as its team for the guidance throughout this project. The authors also thank Dr. Reddikumar Maddipatla for the thoughtful discussions as well as Tim Clarke for making all the custom parts necessary to assemble the human prototype of POCM. Finally, they thank the participants for this study.

Disclosures. The authors declare no conflicts of interest.

Data availability. Data underlying the results presented in this paper are not publicly available at this time but may be obtained from the authors upon reasonable request.

References

1. J. Santodomingo-Rubido, G. Carracedo, A. Suzaki, C. Villa-Collar, S. J. Vincent, and J. S. Wolffsohn, "Keratoconus: An updated review," Cont Lens Anterior Eye **45**(3), 101559 (2022).
2. N. H. Brookes, I. P. Loh, G. M. Clover, C. A. Poole, and T. Sherwin, "Involvement of corneal nerves in the progression of keratoconus," Exp. Eye Res. **77**(4), 515–524 (2003).
3. S. Bonini, P. Rama, D. Olzi, and A. Lambiase, "Neurotrophic keratitis," Eye **17**(8), 989–995 (2003).

4. C. Sarnicola, A. V. Farooq, and K. Colby, "Fuchs endothelial corneal dystrophy: update on pathogenesis and future directions," Eye Contact Lens **45**(1), 1–10 (2019).
5. U. V. Jurkunas, I. Rawe, M. S. Bitar, C. Zhu, D. L. Harris, K. Colby, and N. C. Joyce, "Decreased expression of peroxiredoxins in Fuchs' endothelial dystrophy," Invest. Ophthalmol. Visual Sci. **49**(7), 2956 (2008).
6. F. Bucher, W. Adler, H. C. Lehmann, D. Hos, P. Steven, C. Cursiefen, and L. M. Heindl, "Corneal nerve alterations in different stages of Fuchs' endothelial corneal dystrophy: an in vivo confocal microscopy study," Graefe's Arch. Clin. Exp. Ophthalmol. **252**(7), 1119–1126 (2014).
7. L. A. Hecker, J. W. McLaren, L. A. Bachman, and S. V. Patel, "Anterior keratocyte depletion in Fuchs endothelial dystrophy," Arch. Ophthalmol. **129**(5), 555 (2011).
8. P. Tankam, Z. He, Y. J. Chu, J. Won, C. Canavesi, T. Lepine, H. B. Hindman, D. J. Topham, P. Gain, G. Thuret, and J. P. Rolland, "Assessing microstructures of the cornea with Gabor-domain optical coherence microscopy: pathway for corneal physiology and diseases," Opt. Lett **40**(6), 1113 (2015).
9. K. Wacker, J. W. McLaren, S. R. Amin, K. H. Baratz, and S. V. Patel, "Corneal High-Order Aberrations and Backscatter in Fuchs' Endothelial Corneal Dystrophy," Ophthalmology **122**(8), 1645–1652 (2015).
10. N. Efron, L. Jones, A. J. Bron, E. Knop, R. Arita, S. Barabino, A. M. McDermott, E. Villani, M. D. Willcox, M. Markoulli, and T. I. W. O. C. L. D. members of the, "The TFOS International Workshop on Contact Lens Discomfort: report of the contact lens interactions with the ocular surface and adnexa subcommittee," Invest. Ophthalmol. Visual Sci. **54**(11), TFOS98 (2013).
11. P. B. Morgan, P. J. Murphy, K. L. Gifford, P. Gifford, B. Golebiowski, L. Johnson, D. Makrynioti, A. M. Moezzi, K. Moody, M. Navascues-Cornago, H. Schweizer, K. Swiderska, G. Young, and M. Willcox, "CLEAR - Effect of contact lens materials and designs on the anatomy and physiology of the eye," Cont Lens Anterior Eye **44**(2), 192–219 (2021).
12. R. L. Niederer and C. N. McGhee, "Clinical in vivo confocal microscopy of the human cornea in health and disease," Prog. Retinal Eye Res. **29**(1), 30–58 (2010).
13. J. Zhang, V. Mazlin, K. Fei, A. C. Boccara, J. Yuan, and P. Xiao, "Time-domain full-field optical coherence tomography (TD-FF-OCT) in ophthalmic imaging," Ther. Adv. Chronic Dis. **14**, 204062232311701 (2023).
14. I. N. Petropoulos, G. Ponirakis, A. Khan, H. Gad, H. Almuhannadi, M. Brines, A. Cerami, and R. A. Malik, "Corneal confocal microscopy: ready for prime time," Clin Exp Optom **103**(3), 265–277 (2020).
15. S. Bohn, K. Sperlich, T. Stahnke, M. Schunemann, H. Stolz, R. F. Guthoff, and O. Stachs, "Multiwavelength confocal laser scanning microscopy of the cornea," Biomed. Opt. Express **11**(10), 5689–5700 (2020).
16. J. C. Erie, J. W. McLaren, and S. V. Patel, "Confocal microscopy in ophthalmology," Am. J. Ophthalmol. **148**(5), 639–646 (2009).
17. E. B. Ozgurhan, N. Kara, A. Yildirim, E. Bozkurt, H. Uslu, and A. Demirok, "Evaluation of corneal microstructure in keratoconus: a confocal microscopy study," Am. J. Ophthalmol. **156**(5), 885–893.e2 (2013).
18. A. Zhivov, O. Stachs, J. Stave, and R. F. Guthoff, "In vivo three-dimensional confocal laser scanning microscopy of corneal surface and epithelium," Br. J. Ophthalmol. **93**(5), 667–672 (2009).
19. G. B. van Setten, "Impact of attrition, intercellular shear in dry eye disease: when cells are challenged and neurons are triggered," Int. J. Mol. Sci. **21**(12), 4333 (2020).
20. A. Alharbi and H. A. Swarbrick, "The effects of overnight orthokeratology lens wear on corneal thickness," Invest. Ophthalmol. Visual Sci. **44**(6), 2518 (2003).
21. M. Tavakoli and R. A. Malik, "Corneal confocal microscopy: a novel non-invasive technique to quantify small fibre pathology in peripheral neuropathies," J. Visualized Exp. **47**(47), 1 (2011).
22. D. V. Patel and C. N. McGhee, "Quantitative analysis of in vivo confocal microscopy images: a review," Surv. Ophthalmol. **58**(5), 466–475 (2013).
23. N. Papanas and D. Ziegler, "Corneal confocal microscopy: Recent progress in the evaluation of diabetic neuropathy," *J Diabetes Investig* **6**(4), 381–389 (2015).
24. W. M. Reilly and C. J. Obara, "Advances in confocal microscopy and selected applications," Methods Mol Biol **2304**, 1–35 (2021).
25. K. B. B. Povazay, A. Unterhuber, B. Hermann, H. Sattmann, A.F. Fercher, W. Drexler, A. Apolonski, W.J. Wadsworth, J.C. Knight, P.S.J. Russell, M. Vetterlein, and E. Scherzer, "Submicrometer axial resolution optical coherence tomography," Opt. Lett. **27**(20), 1800–1802 (2002).
26. W. Drexler, "Ultrahigh-resolution optical coherence tomography," J. Biomed. Opt. **9**(1), 47–74 (2004).
27. R. Yadav, K. S. Lee, J. P. Rolland, J. M. Zavislan, J. V. Aquavella, and G. Yoon, "Micrometer axial resolution OCT for corneal imaging," Biomed. Opt. Express **2**(11), 3037 (2011).
28. K. Bizheva, B. Tan, B. MacLelan, O. Kralj, M. Hajialamdari, D. Hileeto, and L. Sorbara, "Sub-micrometer axial resolution OCT for in-vivo imaging of the cellular structure of healthy and keratoconic human corneas," Biomed. Opt. Express **8**(2), 800–812 (2017).
29. M. Ang, M. Baskaran, R. M. Werkmeister, J. Chua, D. Schmidl, V. Aranha Dos Santos, G. Garhofer, J. S. Mehta, and L. Schmetterer, "Anterior segment optical coherence tomography," Prog. Retinal Eye Res. **66**, 132–156 (2018).
30. J. F. de Boer, R. Leitgeb, and M. Wojtkowski, "Twenty-five years of optical coherence tomography: the paradigm shift in sensitivity and speed provided by Fourier domain OCT [Invited]," Biomed. Opt. Express **8**(7), 3248–3280 (2017).
31. B. S. A. Edawaji, I. Gottlob, and F. A. Proudlock, "Anterior chamber measurements in healthy children: a cross-sectional study using optical coherence tomography," Trans. Vis. Sci. Tech. **10**(6), 13 (2021).

32. C. Carnevale, I. Riva, G. Roberti, M. Michelessi, L. Tanga, A. C. Verticchio Vercellin, L. Agnifili, G. Manni, A. Harris, L. Quaranta, and F. Oddone, “Confocal microscopy and anterior segment optical coherence tomography imaging of the ocular surface and bleb morphology in medically and surgically treated glaucoma patients: a review,” Pharmaceuticals **14**(6), 581 (2021).
33. J. A. Izatt, M. R. Hee, G. M. Owen, E. A. Swanson, and J. G. Fujimoto, “Optical coherence microscopy in scattering media,” Opt. Lett. **19**(8), 590–592 (1994).
34. S. Chen, X. Liu, N. Wang, X. Wang, Q. Xiong, E. Bo, X. Yu, S. Chen, and L. Liu, “Visualizing micro-anatomical structures of the posterior cornea with micro-optical coherence tomography,” Sci. Rep. **7**(1), 10752 (2017).
35. V. Mazlin, P. Xiao, E. Dalimier, K. Grieve, K. Irsch, J. A. Sahel, M. Fink, and A. C. Boccara, “In vivo high resolution human corneal imaging using full-field optical coherence tomography,” Biomed. Opt. Express **9**(2), 557–568 (2018).
36. B. Tan, Z. Hosseinaee, L. Han, O. Kralj, L. Sorbara, and K. Bizheva, “250 kHz, 1.5 microm resolution SD-OCT for in-vivo cellular imaging of the human cornea,” Biomed. Opt. Express **9**(12), 6569–6583 (2018).
37. E. Auksorius, D. Borycki, P. Stremplewski, K. Lizewski, S. Tomczewski, P. Niedzwiedziuk, B. L. Sikorski, and M. Wojtkowski, “In vivo imaging of the human cornea with high-speed and high-resolution Fourier-domain full-field optical coherence tomography,” Biomed. Opt. Express **11**(5), 2849–2865 (2020).
38. V. Mazlin, P. Xiao, J. Scholler, K. Irsch, K. Grieve, M. Fink, and A. C. Boccara, “Real-time non-contact cellular imaging and angiography of human cornea and limbus with common-path full-field/SD OCT,” Nat. Commun. **11**(1), 1868 (2020).
39. S. Khan, K. Neuhaus, O. Thaware, S. Ni, M. J. Ju, T. Redd, D. Huang, and Y. Jian, “Corneal imaging with blue-light optical coherence microscopy,” Biomed. Opt. Express **13**(9), 5004–5014 (2022).
40. F. Beer, A. Wartak, N. Pircher, S. Holzer, J. Lammer, G. Schmidinger, B. Baumann, M. Pircher, and C. K. Hitzenberger, “Mapping of corneal layer thicknesses with polarization-sensitive optical coherence tomography using a conical scan pattern,” Invest. Ophthalmol. Visual Sci. **59**(13), 5579–5588 (2018).
41. G. R. Hartl, A. Parmar, G. Sharma, and K. Singh, “Cross-polarized optical coherence tomography system with unpolarized light,” Photonics **9**(2), 76 (2022).
42. M. Villiger, C. Pache, and T. Lasser, “Dark-field optical coherence microscopy,” Opt. Lett. **35**(20), 3489 (2010).
43. S. Sridhar and A. Da Silva, “Enhanced contrast and depth resolution in polarization imaging using elliptically polarized light,” J. Biomed. Opt **21**(7), 071107 (2016).
44. K. S. Lee, A. C. Akcay, T. Delemos, E. Clarkson, and J. P. Rolland, “Dispersion control with a Fourier-domain optical delay line in a fiber-optic imaging interferometer,” Appl. Opt. **44**(19), 4009–4022 (2005).
45. R. Maddipatla and P. Tankam, “Development of high-speed, integrated high-resolution optical coherence microscopy and dual-channel fluorescence microscopy for the simultaneous co-registration of reflectance and fluorescence signals,” Optics and Lasers in Engineering **149**, 106823 (2022).
46. L. Han, B. Tan, Z. Hosseinaee, L. K. Chen, D. Hileeto, and K. Bizheva, “Line-scanning SD-OCT for in-vivo, non-contact, volumetric, cellular resolution imaging of the human cornea and limbus,” Biomed. Opt. Express **13**(7), 4007–4020 (2022).
47. L. Z. Cai, Q. Liu, and X. L. Yang, “Generalized phase-shifting interferometry with arbitrary unknown phase steps for diffraction objects,” Opt. Lett. **29**(2), 183 (2004).
48. J. M. Schmitt and S. H. Xiang, “Cross-polarized backscatter in optical coherence tomography of biological tissue,” Opt. Lett. **23**(13), 1060 (1998).
49. S. Jiao and M. Ruggeri, “Polarization effect on the depth resolution of optical coherence tomography,” J. Biomed. Opt. **13**(6), 060503 (2008).
50. D. A. Zimnyakov, Y. P. Sinichkin, P. V. Zakharov, and D. N. Agafonov, “Residual polarization of non-coherently backscattered linearly polarized light: the influence of the anisotropy parameter of the scattering medium,” Waves in Random Media **11**(4), 395–412 (2001).
51. M. Munter, M. Pieper, T. Kohlfaerber, E. Bodenstorfer, M. Ahrens, C. Winter, R. Huber, P. Konig, G. Huttmann, and H. Schulz-Hildebrandt, “Microscopic optical coherence tomography (mOCT) at 600 kHz for 4D volumetric imaging and dynamic contrast,” Biomed. Opt. Express **12**(10), 6024–6039 (2021).
52. Y. Miao, J. Song, and M. J. Ju, “Image-based cross-calibration method for multiple spectrometer-based OCT,” Opt. Lett. **47**(19), 5096–5099 (2022).
53. S. Murali, K. P. Thompson, and J. P. Rolland, “Three-dimensional adaptive microscopy using embedded liquid lens,” Opt. Lett. **34**(2), 145 (2009).
54. H. S. Ee and R. Agarwal, “Tunable metasurface and flat optical zoom lens on a stretchable substrate,” Nano Lett. **16**(4), 2818–2823 (2016).
55. R. A. Leitgeb, M. Villiger, A. H. Bachmann, L. Steinmann, and T. Lasser, “Extended focus depth for Fourier domain optical coherence microscopy,” Opt. Lett. **31**(16), 2450 (2006).
56. Y. Z. Liu, F. A. South, Y. Xu, P. S. Carney, and S. A. Boppart, “Computational optical coherence tomography [Invited],” Biomed. Opt. Express **8**(3), 1549–1574 (2017).